Engineering Fracture Mechanics 303 (2024) 110118

Contents lists available at ScienceDirect

Engineering Fracture Mechanics

journal homepage: www.elsevier.com/locate/engfracmech

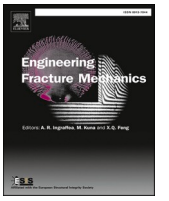

# Fracture assessment of polyamide 12 (PA12) specimens fabricated via Multi Jet Fusion™ in the presence of geometrical discontinuities

Andrea Avanzini [a,*], Matteo Tomasoni [a,b], Zhuo Xu [b], Filippo Berto [c], Nima Razavi [b,*]

[a] Department of Mechanical and Industrial Engineering, University of Brescia, via Branze 38, 25123 Brescia, Italy
[b] Department of Mechanical and Industrial Engineering, Norwegian University of Science and Technology (NTNU), Verkstedteknisk, 241B, Gløshaugen, Richard Birkelands vei 2b, Trondheim, Norway
[c] Department of Chemical Engineering Materials Environment, SAPIENZA – UNIVERSITA' DI ROMA, Via Eudossiana, 18, 00184 Roma, Italy

ARTICLE INFO

*Keywords:*
Additive Manufacturing
Polyamide 12
Notch
Mode mixity
ASED

ABSTRACT

This study aims to study the fracture resistance of additively manufactured polyamide 12 (PA12), specifically when subjected to notches and cracks, and how it varies with the printing direction using Multi Jet Fusion (MJF). The methodology involved conducting tensile tests on V-notched samples, with a focus on different combinations of opening angle (0°-120°) and tip radius (0.2–2 mm). The findings revealed that the sensitivity to the notch opening angle decreased with an increase in the notch tip radius. Furthermore, the fracture resistance for different mode mixities was examined using semi-circular bend (SCB) specimens, with the crack angle varied between 0° and 53°. The results demonstrated two distinct fracture behaviours, namely brittle and ductile, depending on the crack angle. Theoretical analyses revealed that with appropriate tuning, average strain energy density (ASED) can predict the load capacity of notched and cracked PA12 parts manufactured with MJF, within an error range of ± 20 %.

## 1. Introduction

ISO/ASTM 52900:2021 defines additive manufacturing (AM) as the creation of physical objects by material addition accordingly to a 3D model specification and groups the AM technologies into seven processes: Binder Jetting, Direct Energy Deposition, Material Extrusion, Material Jetting, Powder Bed Fusion, Sheet Lamination and Vat Polymerization [1]. Multi Jet Fusion (MJF) belongs to powder bed fusion (PBF) processes and shares most of their benefits as the high accuracy, precision and the capability to realize overhanging structures without needing any supporting framework [2]. Briefly, the MJF 3D printing process comprises three steps: first, a thin layer of polymer powder is pre-heated and spread across the building platform. Next, the fusing agent is deposited where the powder fusion is meant to happen, and the detailing agent is applied to the edges of the part. Finally, an array of infrared lamps delivers energy to fuse the material and form a complete layer. The process is then repeated until the completion of the part. In comparison with Binder Jetting, where a single binding agent is jetted, MJF technology uses two agents, and the polymer chains entangle to fuse rather than bind or glue the layers. Differently from SLS, which uses a laser to sinter the powder with a point-by-point approach, MJF uses an inkjet array to jet fusing and detailing agents, and array lamps enable the printing of a complete layer at the

* Corresponding authors.
*E-mail addresses:* andrea.avanzini@unibs.it (A. Avanzini), nima.razavi@ntnu.no (N. Razavi).

https://doi.org/10.1016/j.engfracmech.2024.110118
Received 12 January 2024; Received in revised form 26 April 2024; Accepted 27 April 2024
Available online 4 May 2024

**Nomenclature**

| | |
|---|---|
| AM | Additive Manufacturing |
| ASED | Average Strain Energy Density |
| DIC | Digital Image Correlation |
| e | Average error |
| E | Young's Modulus |
| ELSE | Total elastic strain energy in the elements of the control volume |
| EMC | Equivalent Material Concept |
| EVOL | Current element volume |
| FEA | Finite Element Analysis |
| $F_{exp}$ | Average Experimental failure |
| $F_{Fail}$ | Failure load (experimental) |
| $F_{fea}$ | Load applied in FEA (arbitrary) |
| $F_{th}$ | Theoretical failure load |
| H | Ramberg-Osgood parameter (stress) |
| $K_I$ | Mode I stress intensity factor |
| $K_{IC}$ | Fracture Toughness |
| $K_{II}$ | Mode II stress intensity factor |
| $M_e$ | Mode mixity parameter |
| MJF | Multi Jet Fusion |
| n | Ramberg-Osgood parameter (exponent) |
| PBF | Powder Bed Fusion |
| PA12 | Polyamide 12 |
| q | Control volume angular parameter |
| $r_0$ | Control volume distance parameter |
| $R_0$ | Critical radius |
| SCB | Semi-Circular Bend (specimens) |
| SIF | Stress Intensity Factor |
| SLS | Selective Laser Sintering |
| t | Specimen thickness (dogbone gage section) |
| TCD | Theory of Critical Distances |
| $t_m$ | Specimen thickness (V-notch, net section) |
| $T_m$ | Melting point temperature |
| w | Specimen width (dogbone gage section) |
| $W_c$ | Critical strain energy density |
| $W_{fea}$ | Strain energy density, numerical |
| $w_m$ | Specimen width (V-notch, net section) |
| $2\alpha$ | Notch opening angle |
| $\varepsilon_b$ | Elongation at break |
| $\nu$ | Poisson's Ratio |
| $\theta$ | Crack angle (SCB specimens) |
| $\rho$ | Notch tip radius |
| $\sigma_{fail}$ | Failure stress (notched specimens, nominal dimensions) |
| $\sigma_{(fail,m)}$ | Failure stress (notched specimens, measured dimensions) |
| $\sigma_{UTS}$ | Ultimate Tensile Strength |

same time. One of the most extensively used polymer for MJF is polyamide 12 (PA12) [3,4], which is an engineering semi-crystalline polymer which guarantees good processability, a relatively high melting point of $\approx 180\,^{\circ}C$, a large processing window, has low density, high elongation at break and good strength [5,6]. For additively manufactured parts, this layer-by-layer 3D printing processes may result in the presence of defects, with detrimental effects on the strength and fracture properties, and in anisotropic mechanical behavior. Therefore, each AM technology has to be deeply analyzed to evaluate its influence on the mechanical performance of the printed parts. As a consequence, although MJF is still a recently developed technology, many studies have already been conducted to date, investigating mechanical performances of PA12 [7–13], also in comparison with Selective Laser Sintering (SLS), the main competitor technology of MJF, as in [14]. Multiscale characterizations of mechanical and tribological properties were also reported [15], highlighting that printing orientation plays a broad role in performance optimization, dictating the mechanical properties and the wear resistance of the printed component.

On the other hand, the evaluation of the structural integrity of additively manufactured polymeric parts, especially when dealing with high local curvatures or complex loading modes, necessarily requires knowledge of material resistance in the presence of internal

defects and geometrical discontinuities. For the more common combinations of process and polymeric materials, like ABS manufactured via Fused Deposition Modelling (FDM), the current literature already provides several sources of information about notched components and fracture behavior. For example, the application of different fracture theories were discussed in [16,17] and investigations on mixed-mode fracture were presented in [18,19]. Restricting the focus on AM PA12, the current knowledge is more limited, and the investigations reported in the literature mostly dealt with SLS process. In [20] failure of SLS polyamide 12 notched samples at high loading rates was considered, to verify how characteristic stress and length parameters for the Theory of Critical Distances (TCD) were affected by strain rates. The effect of temperature on the fracture behavior of SLS PA12 was considered in [21], showing that $J_{IC}$ values of PA12 were similar at − 50 °C and at 23 °C and much lower than at 50 °C. Particularly relevant is also a recent study [22], in which the fracture behavior of SLS PA12 was assessed through mixed-mode fracture tests and J-integral analyses, showing that the material exhibited higher resistance under shearing mode loading. Notably, for PA12 manufactured using MJF, this field of investigation remains relatively unexplored, being limited to [23], where the equivalent material concept (EMC) combined with the J-integral criterion was considered, and to [24] in which TCD was employed and a good agreement between experimental and numerical results for MJF PA12 was reported. However, to the best of the authors' knowledge, a systematic investigation for the assessment of an optimal implementation of fracture prediction criterion is still missing, and regarding the fracture resistance of cracked MJF PA12 components, no direct measurements have been published yet, neither for mode I loading, nor for more complex load cases resulting in mode mixities. This paper aims to evaluate the fracture resistance of PA12 produced via MJF in the presence of geometrical discontinuities, such as notches and cracks, employing mechanical tests, complemented with digital image correlation (DIC) analyses, numerical simulations, and local failure prediction approaches. To this aim, plain dogbone samples were tested to evaluate the static performance in different printing directions. V-Notched samples were statically tested changing opening angle and tip radius and different mode mixities were considered for the semi-circular bend (SCB) specimens, varying the crack angle and the printing direction. In all the cases, several samples were tested to ensure the statistical meaningfulness of the results. At the same time, numerical analyses have been carried out to investigate the application of the average strain energy density (ASED) criterion for the different examined configurations.

## 2. Materials and methods

### 2.1. Fabrication of the specimens

The specimens were provided by ELMEC S.p.a. and fabricated via MJF with an HP-MJF-5200 system from Hewlett-Packard™ using the recommended process parameters by HP. The printer was fed with a PA12 powder with a melting point $T_m$ of 187 °C, bulk density of 0.425 g/cm$^3$ and a particle size of 60 μm. The geometries of the different tested samples are reported in Fig. 1(a–c). The evaluation of mechanical properties (i.e. the Young's modulus (E), the Poisson's ratio ($\nu$), the Ultimate Tensile Strength ($\sigma_{UTS}$) and elongation at break $\varepsilon_b$) was made using plain dogbone samples, which were printed either flat on the XY plane or vertically (X direction and Z direction respectively, according to ISO/ASTM52900-21 [1] as shown in Fig. 1(d).

The density of the material was evaluated using Archimede's principle, and measurements resulted in an average value of 1.0001 ± 0.002 g/cm$^3$. Negligible differences were found for samples in the Z and XY printing directions. By comparing theoretical density and experimental measurements, an estimated porosity of 1.98 ± 0.19 % was determined, assuming for MJF PA12 a full-density value of 1.020 g/cm$^3$ [25]. The porosity level is comparable with literature; in particular, in [25] a systematic investigation on the porosity of MJF parts showed a range between 0.5 and 2 %. However, the range of data reported in the literature is quite large, from values lower than 1 % [10] up to 6.75 % [14], possibly as a consequence of the method employed. It should also be underlined that an accurate assessment of internal porosity is not trivial, and that the theoretical density may slightly vary depending on the ratio between amorphous and crystalline phases.

To assess the effect of stress concentration on the load bearing capacity of specimens, notched samples were tested considering

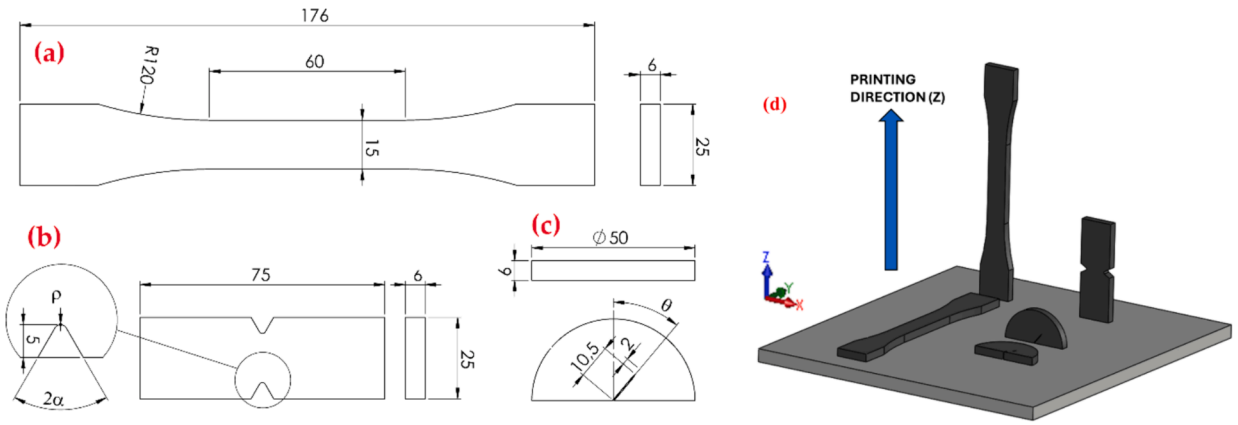


**Fig. 1.** Specimen dimensions (units mm): (a) Dogbone; (b) V-Notched; (c) Semi-Circular Bend; d) Reference system.

different opening angles ($2\alpha = 0°,30°,60°,90°,120°$) and tip radius ($\rho = 0.2,1,2$ mm), limiting in this case the study to the Z direction, for a total of 15 combinations. Fracture resistance and mode mixities were investigated using SCB specimens, printed as disks, on X and Z directions. The printed specimens included a proper pre-crack notch and were afterward laser cut into half-disks along their diameter using a Gravograph LS1000XP machine, and eventually refined along the cut surface using a Buehler Metaserv 250 twin grinder-polisher machine and 80 grit sandpaper. The crack was created by cutting the pre-existing notch tip by pushing a razor blade inside the material with a hammer. The pre-cracking procedure was applied by placing SCB specimens in a table vise, with appropriate markings on the specimen to make sure the notch was vertical. Since using the hammer may cause uncontrolled pre-crack length, two hard steel restricting plates were placed on both sides of the specimen, allowing to reach more precisely the desired propagation length of the pre-crack (2 mm). All pre-crack lengths were measured after the fracture tests and the values showed good consistency ($12.4 \pm 0.3$ mm overall average value and standard deviation). Four crack angles ($\theta = 0°,15°,30°,53°$) were used, leading to eight different conditions. A fair number of specimens was tested for each condition (5 for dogbone and notched and 4 for SCB) to ensure the statistical meaningfulness of the results obtained. The geometrical accuracy of the printed parts was evaluated using different instruments. The linear dimensions of the specimens were checked using a Mitutoyo Digimatic 150 mm ABSOLUTE AOS 500–181-30 calliper, while the notch radii were measured with a Hirox RH-2000 3D Digital Microscope. Regarding the SCB samples, the prescribed crack length (a) was determined considering half of the sample radius measured perpendicularly to the straight surface; then, its actual dimension on each sample was measured after their break. The measurement of crack angle and notch opening angle was overlooked. Dimensional checks showed in general a very a good accuracy level, with somewhat larger deviations from nominal values only for the $\rho = 0.2$ mm condition.

### 2.2. Mechanical testing

The testing campaign was conducted using an MTS Criterion Mode 42 with a load cell capacity of 5kN. Plain dogbone and notched specimens were tested under static tensile loading, while SCB specimens were tested under three-point bending with a roller span of 36 mm and a roller diameter of 10 mm. The rollers had freedom of spin along their axis to avoid unnecessary constraints from boundary conditions to the test specimens. Each test was conducted at a 2 mm/min displacement rate and the data acquisition was set to 10 Hz. Digital image correlation (DIC) was used for all the tests on dogbone samples and for one specimen per each condition of the notched and SCB specimens. The software Vic-Snap and Vic-2D-7 were used for the single-camera acquisition and the post-processing of the images, respectively. The acquisition frequency was set to 5 Hz, the subset size was set to the suggested value and the subset step was set to 7 for the plain dogbone analysis while it was set to 3 for the other conditions, which required a finer discretization of the region of interest to capture the strain gradient more precisely. The strain computation was carried out with an engineering tensor and a filter size of 15. The remaining settings were left to their default values. The fractographic analyses were conducted with a Hirox RH-2000 3D Digital Microscope using its 3D automatic tiling procedure. Each picture was taken using a magnification of 35x. The pictures were taken on grayscale and the image contrast and brightness were set to ensure the best possible result for each sample.

### 2.3. Numerical modelling

The finite element analyses were performed to assess the fracture resistance, stress intensity, and stress concentration factors values. For each specimen geometry, a 2D plane strain model was developed; the material properties were set from the experimental data, considering the average values. We assumed a linear-elastic isotropic model. The finite element models were implemented into the commercial software Abaqus/CAE. For notched specimens' models, the symmetry of geometry, loads and boundary conditions was considered, sketching only a quarter of the parts. Two different partitions and mesh were employed: for the stress concentration factors analyses, quadratic CP8 structured elements were employed far from the notch tip, whereas a free mesh control was applied in the notch region. For the strain energy density evaluation, free CP8 elements were used in all the models and the partition was changed, including a circular shaped control volume around the notch tip itself. In both cases, the applied load was unitary. As regards the SCB models, quadratic CP8 free elements were applied to the model beside the control volume around the crack tip, where quad-dominant CP8/CP6 sweep elements were employed. The crack was modelled with contour integral. For mode I stress intensity factor $K_I$ evaluation, the load was set to the average failure load (from the experimental campaign). The load was unitary for the strain energy density evaluation, and the radius was set according to the formulation in theoretical background section (section 2.4). The modelling of the contact between the sample and the rollers was overlooked.

### 2.4. Theoretical background

The Average Strain Energy Density (ASED) criterion in often used for fracture prediction of cracked and notched specimens. While for in-depth review of the criterion and its application to static and fatigue load conditions the interested reader may refer to [26,27,28], brief recalls will be provided for a better understanding of the procedure followed in the present study to assess its applicability to MJF PA12. The ASED criterion is a local approach that allows the prediction of static and fatigue failures. Hereafter, the static failure prediction method will be considered, since it is the one employed during the research. The criterion predicts the component's failure when the strain energy density inside a control volume around the geometrical feature of interest reaches the critical. The key values that should be computed to apply the criterion are the critical strain energy density ($W_c$) and the critical radius ($R_0$) value. For an ideally brittle material, $W_c$ can be evaluated as per eq. (1):

$$W_c = \frac{\sigma_{UTS}^2}{2E} \tag{1}$$

The critical radius is computed from eq. (2) as follows:

$$R_0 = \frac{(1+\nu)(5-8\nu)}{4\pi}\left(\frac{K_{IC}}{\sigma_{UTS}}\right)^2 \tag{2}$$

For the present study, the mechanical properties needed for both the equations were obtained from dogbone experimental tests' results, besides the fracture toughness $K_{IC}$ which, is numerically evaluated from the experimental results of SCB specimens. The position of the control volume is defined as shown in Fig. 2.

The control volume is related to the geometrical discontinuity type, by the parameters $r_0$ and q, defined by eq. (3) and eq. (4) respectively as:

$$r_0 = \frac{\rho(q-1)}{q} \tag{3}$$

$$q = \frac{2\pi - 2\alpha}{\pi} \tag{4}$$

Then, the control volume has to be implemented in the finite element model to evaluate the strain energy density ($W_{fea}$) inside it when an arbitrary load ($F_{fea}$) is applied. The theoretical failure load ($F_{th}$) is the load for which the average strain energy density $W_{fea}$ is equal to the critical value $W_c$. Therefore, $F_{th}$ can be computed from the simple proportion (eq. (5)):

$$F_{th} = F_{fea}\sqrt{\frac{W_c}{W_{fea}}} \tag{5}$$

It should be noted that a few alternative methods of application of the ASED criterion are available, which do not require knowledge of $K_{IC}$, essentially based on iterative procedures for numerical calibration of the control volume. In the present work, further to the theoretical method previously described, we considered two different approaches, which are exemplified in Fig. 3.

The first alternative to the direct computation of the critical radius through the theoretical formulation will be referred to as "Sharp notch vs. $W_c$" and it is based on the data gathered from the tensile tests of dogbone and notched samples and an iterative procedure. By applying the mean value of the experimental failure load for an arbitrary configuration ($\rho = 0.2$ mm, $2\alpha = 30^\circ$ in our case), we can find the value of $W_{fea}$ numerically as a function of $R_0$. The intersection with $W_c$, which is an horizontal straight line defined by equation (1), will determine the actual value of the control radius.

The second alternative ("Sharp vs. Blunt notch") is based only on the tensile test results on notched samples. This method calculates both the critical radius and the critical value of the ASED iteratively.

The procedure is similar to the previous one, but it considers two different geometries, a sharp and a blunt one ($\rho = 0.2$ mm,$2\alpha = 30^\circ$ and $\rho = 2$ mm, $2\alpha = 120^\circ$ in our cases). The applied load is the respective average value of failure load from the experimental results. By varying the control radius by trials and errors, the intersection point of the two curves will be eventually found; its abscissa is the critical radius, while its ordinate is the critical strain energy density $W_c$.

Finally, considering tests on SCB samples, one of the main goals was to evaluate the fracture resistance spacing from Mode I up to Mode II, to have a more complete view of the material's mechanical properties.

To this aim, it is convenient to define the elastic mode mixity parameter $M_e$ as per eq. (6):

$$M_e = \frac{2arctan\frac{K_I}{K_{II}}}{\pi} \tag{6}$$

where $K_I$ and $K_{II}$ are the stress intensity factors (SIF) for mode I and mode II respectively. $M_e$ may vary between 1 (pure mode I) and 0 (pure mode II).

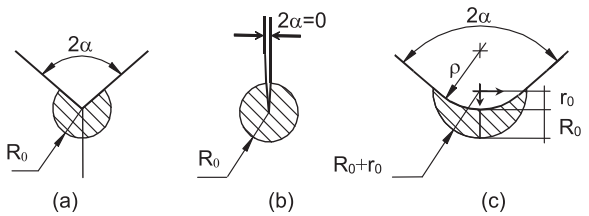


**Fig. 2.** Critical volume (area) under mode I loading: a) sharp V-notch, b) crack, c) blunt V-notch (Adapted [26]).

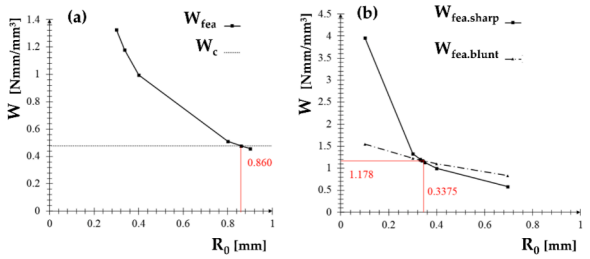


**Fig. 3.** (a) "Sharp notch vs. Wc", (b) "Sharp vs. Blunt notch".

## 3. Results

### 3.1. Tensile properties

The stress–strain curves of the tested specimens with different printing orientations are shown in Fig. 4. Complete results for all tensile tests can be found in Table 1, including material parameters for fitting with a Ramberg-Osgood equation [29].

Considering data reported in Table 1, t and w are the measured thickness and width in the gage section, respectively, which must be compared to the nominal values. E is the elastic modulus, $\nu$ is the Poisson's ratio, $\varepsilon_b$ is the elongation at break and $\sigma_{UTS}$ is the ultimate tensile strength.

The case where $\nu$ is not reported indicates that the data obtained from the DIC were unreliable for its calculation. H and n are the plastic parameters for the Ramberg-Osgood model, which were not reported in those cases where the breakage occurred in the linear elastic region.

Overall, the tests showed good repeatability, especially for the initial portion of the curve, with higher dispersion for elongation at break $\varepsilon_b$ and UTS. The results showed a limited influence of the building direction on the mechanical response, except for a reduced strain at failure ($\varepsilon_b$) for the specimens printed vertically and are in line with the data reported in literature for MJF PA12 [2,7,8,10,11,14,24].

### 3.2. Notched specimens

#### 3.2.1. Experimental results

The complete results for all the tests can be found in Table 2, whereas a visual representation of the failure load trends among the considered configurations, is given in Fig. 5 (a,b,c) charts.

The measured thickness and width of the net section are called $t_m$ and $w_m$, respectively. The failure load ($F_{fail}$), was used to compute the stress in the net section for the nominal values of thickness and width ($\sigma_{fail}$) and the measured ones ($\sigma_{(fail,m)}$).

It should be underlined that stress values do not consider the stress concentration around the notch tip. The values of failure load $F_{Fail}$ ranged approximately between 2000 and 3500 N but different trends could be noticed depending on the combination of notch tip radius $\rho$ and opening angles $2\alpha$.

In particular, for the smallest value of $\rho = 0.2$ mm the failure load increased more markedly with the opening angle, whereas for $\rho = 2$ mm this trend is less apparent and higher dispersion of the data can be noticed.

This could suggest a competitive role between notch effect and defects, with these latter being more relevant when the stress concentration effect resulting from the notch is lower.

#### 3.2.2. Theoretical predictions

In order to apply the ASED criterion for $F_{fail}$ prediction, the critical values of $W_c$ and the control radius $R_0$ must be determined. Following the theoretical procedure described in section 2.4, combined with the data obtained from experimental testing, equations

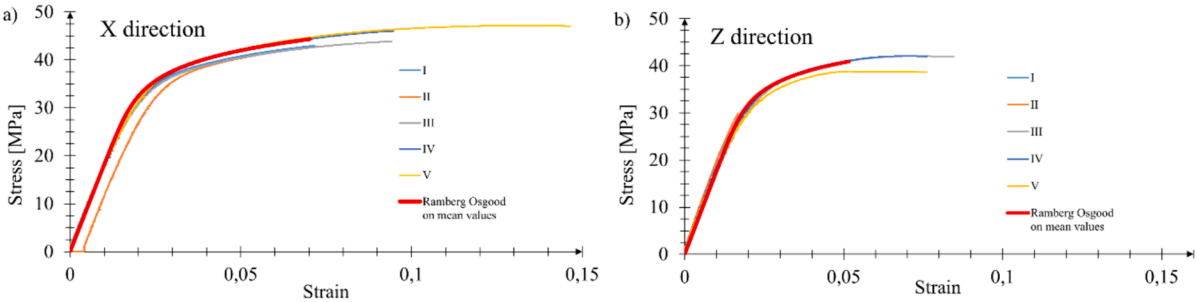


**Fig. 4.** Engineering Stress vs strain curves from the dogbone specimens printed in different orientations: (a) X, (b) Z.

**Table 1**
Results of tensile tests.

| Orientation | Nr. | t mm | w mm | E MPa | H MPa | n | $\varepsilon_B$ % | $\sigma_{UTS}$ MPa | $\nu$ |
|---|---|---|---|---|---|---|---|---|---|
| **X** | I | 5.91 | 14.82 | 1754.2 | 59.82 | 0.0936 | 7.18 | 42.97 | 0.41 |
| | II | 5.95 | 14.87 | 1853.5 | 61.07 | 0.106 | 6.21 | 41.83 | |
| | III | 5.93 | 14.73 | 1818.7 | 59.43 | 0.0939 | 9.44 | 43.83 | 0.41 |
| | IV | 6.06 | 14.86 | 1821.7 | 62.42 | 0.1061 | 9.47 | 46.01 | 0.38 |
| | V | 6.02 | 14.71 | 1830.5 | 60.75 | 0.0917 | 14.64 | 47.17 | 0.4 |
| | Mean | | | 1815.7 | 60.7 | 0.102 | 9.39 | 44.36 | 0.4 |
| **Z** | I | 6.08 | 15.25 | 1901.3 | | | 1.4 | 25.7 | 0.43 |
| | II | 5.92 | 15.07 | 1970.7 | | | 1.67 | 29.84 | 0.35 |
| | III | 5.91 | 14.91 | 1750.4 | 58.5 | 0.096 | 8.46 | 42.05 | 0.35 |
| | IV | 5.88 | 14.94 | 1799.1 | 58.24 | 0.0961 | 7.61 | 42.06 | 0.36 |
| | V | 5.93 | 14.88 | 1743.6 | 55.66 | 0.0938 | 7.61 | 38.79 | 0.36 |
| | Mean | | | 1764.4 | 57.47 | 0.0953 | 7.9 | 40.97 | 0.36 |

(1) and (2) yielded values of $W_c = 0.4756$ N mm/mm$^3$ and $R_0 = 1.33$ mm.

Note that the required value of fracture toughness was determined from numerical analyses of SCB test presented in section 2.3, which yielded $K_{IC} = 101.1$ MPa mm$^{0.5}$ for X direction (flat printed) and $K_{IC} = 98.15$ MPa mm$^{0.5}$ for Z direction (vertically printed).

The application of the iterative procedure "Sharp notch vs. $W_c$" resulted in values of $W_c = 0.496$ N mm/mm$^3$ and $R_0 = 0.860$ mm, whereas the procedure "Sharp vs. Blunt notch" procedure resulted in values of $W_c = 1.178$ N mm/mm$^3$ and $R_0 = 0.3375$ mm respectively.

The results of the predictions obtained by applying the different methods are comparatively reported in Fig. 6 for each geometrical configuration, choosing the ratio $F_{exp}/F_{th}$ as an indicator of prediction precision.

Complete tables with all the values for all the tested configurations are available in Table 3.

The average error and standard deviation of the methods for the theoretical method was $e = -4.6 \pm 17.3$ %. The iterative procedure "Sharp notch vs. $W_c$" resulted in $e = 15.1 \pm 20.0$ % whereas for the "Sharp vs. Blunt notch" the minimum error was obtained, $e = 4.3 \pm 15.8$ %, showing that this last method is the more accurate one.

### 3.3. Semi-circular bend specimens

#### 3.3.1. Experimental results

The results of mixed mode fracture tests are presented in form of failure load in Fig. 7 (a,b) as a function of printing direction and in tabular form in Table 4.

While the failure load expected trend would be monotonic increasing with crack angle, the results obtained slightly deviated, with a failure load drop in the $\theta = 15^\circ$ configurations, for both the printing directions. The tested specimens displayed two different failure behaviors, as shown for example in Fig. 8. Some specimens failed suddenly once they reached the failure load (i.e. "brittle" behaviour). In other cases, once the load reached its peak value under compression, the crack propagated slowly and exhibited a stable behaviour (i.e. "ductile").

It should be noted that due to some issues arised during the experimental campaign (i.e. limitations on the maximum achievable crack length and indentation of the samples) a pure mode II condition could not be reached and a minimum value of $M_e = 0.5$ could be achieved. Note that Table 4 does not yield any result for the XY – $\theta = 53^\circ$ samples: all of them jumped out the machine during the test once the load had reached up to 2500 N. The residual deformation on these specimens prevented us from re-run the tests and broke them. Ductile failures are underlined.

#### 3.3.2. Experimental results and theoretical predictions

Substituting in equations (1) and (2) the average values of material properties from the experimental tests and we obtain the critical SED and the critical radius for both the printing directions. For XY direction this yielded values of $W_c = 0.5419$ N mm/mm$^3$ and $R_0 = 1.064$ mm, whereas for Z direction they are the same previously reported. The theoretical value of failure load for each configuration are available in Table 5, whereas the juxtaposition of the results from the experimental campaign and the theoretical ones is visually presented in the chart of Fig. 9 (a,b).

As it can be seen, the configuration with 15° crack angle has significantly higher error than the other cases in which the failure load, besides a couple of outliers, is well predicted by the criterion. This deviation between experimental and theoretical results is related to the former one. As reported before, the 15° configuration shows an unexpected trend where the failure load is decreased if compared with the 0° one, which is not predicted by the ASED criterion.

**Table 2**
Results of tests on notched specimens.

| ρ | 2α | Nr. | $w_m$ | $t_m$ | $F_{fail}$ | $\sigma_{fail}$ | $\sigma_{fail,m}$ | ρ | 2α | Nr. | $w_m$ | $t_m$ | $F_{fail}$ | $\sigma_{fail}$ | $\sigma_{fail,m}$ | ρ | 2α | Nr. | $w_m$ | $t_m$ | $F_{fail}$ | $\sigma_{fail}$ | $\sigma_{fail,m}$ |
|---|---|---|---|---|---|---|---|---|---|---|---|---|---|---|---|---|---|---|---|---|---|---|---|
| mm | deg | | mm | mm | N | MPa | MPa | mm | deg | | mm | mm | N | MPa | MPa | mm | deg | | mm | mm | N | MPa | MPa |
| 0.2 | 0 | I | 15.20 | 5.99 | 2121.5 | 23.57 | 23.30 | 1 | 0 | I | 15.03 | 5.96 | 2553.1 | 28.37 | 28.50 | 2 | 0 | I | 14.97 | 6.01 | 1613.4 | 17.93 | 17.93 |
| | | II | 14.94 | 6.02 | 2129.5 | 23.66 | 23.68 | | | II | 15.00 | 5.94 | 2959.4 | 32.88 | 33.21 | | | II | 15.01 | 6.04 | 3060.2 | 34.00 | 33.75 |
| | | III | 15.03 | 5.97 | 2130.7 | 23.67 | 23.75 | | | III | 14.93 | 5.89 | 2844.6 | 31.61 | 32.35 | | | III† | 14.96 | 6.12 | 3230.6 | 35.90 | 35.29 |
| | | IV† | 14.97 | 5.97 | 2338.8 | 25.99 | 26.17 | | | IV† | 14.94 | 5.92 | 2278.1 | 25.31 | 25.76 | | | IV | 14.98 | 6.02 | 2524.1 | 28.05 | 27.99 |
| | | V | 15.16 | 5.96 | 1974.9 | 21.94 | 21.86 | | | V | 15.06 | 6.01 | 2672.2 | 29.69 | 29.52 | | | V | 14.94 | 5.95 | 2309.1 | 25.66 | 25.98 |
| | | Mean | | | 2139.1 | | | | | Mean | | | 2661.5 | | | | | Mean | | | 2547.5 | | |
| | 30 | I | 15.15 | 5.89 | 2389.2 | 26.55 | 26.78 | | 30 | I | 15.02 | 5.94 | 2770.9 | 30.79 | 31.06 | | 30 | I | 14.94 | 5.99 | 2497.4 | 27.75 | 27.91 |
| | | II | 14.98 | 5.84 | 2406.9 | 26.74 | 27.51 | | | II | 14.89 | 5.93 | 2950.1 | 32.78 | 33.41 | | | II | 14.95 | 5.96 | 2649.2 | 29.44 | 29.73 |
| | | III† | 14.92 | 5.93 | 2020.6 | 22.45 | 22.84 | | | III† | 15.15 | 6.19 | 2997.9 | 33.31 | 31.97 | | | III† | 15.03 | 6.03 | 3190.7 | 35.45 | 35.21 |
| | | IV | 15.05 | 5.91 | 2715.4 | 30.17 | 30.53 | | | IV | 14.94 | 5.93 | 2558.3 | 28.43 | 28.88 | | | IV | 15.09 | 6.08 | 3549.7 | 39.44 | 38.69 |
| | | V | 15.53 | 6.18 | 2986.5 | 33.18 | 31.12 | | | V | 15.10 | 6.04 | 2332.0 | 25.91 | 25.57 | | | V | 15.03 | 5.98 | 2917.1 | 32.41 | 32.46 |
| | | Mean | | | 2503.7 | | | | | Mean | | | 2721.8 | | | | | Mean | | | 2960.8 | | |
| | 60 | I | 15.58 | 5.99 | 2145.5 | 23.84 | 22.99 | | 60 | I | 14.91 | 6.00 | 2656.6 | 29.52 | 29.70 | | 60 | I | 14.99 | 6.07 | 3701.5 | 41.13 | 40.68 |
| | | II | 15.16 | 5.98 | 2535.8 | 28.18 | 27.97 | | | II | 14.97 | 5.95 | 2612.8 | 29.03 | 29.33 | | | II | 14.97 | 6.00 | 2677.1 | 29.75 | 29.81 |
| | | III† | 14.95 | 5.94 | 2446.2 | 27.18 | 27.55 | | | III† | 14.99 | 5.90 | 2720.6 | 30.23 | 30.76 | | | III† | 14.94 | 6.02 | 3279.5 | 36.44 | 36.46 |
| | | IV | 14.96 | 6.05 | 2986.2 | 33.18 | 32.99 | | | IV | 14.98 | 5.92 | 3102.4 | 34.47 | 34.98 | | | IV | 14.95 | 5.92 | 2250.0 | 25.00 | 25.42 |
| | | V | 14.86 | 5.99 | 2374.0 | 26.38 | 26.67 | | | V | 15.00 | 5.92 | 3042.4 | 33.80 | 34.26 | | | V | 14.90 | 5.95 | 3035.5 | 33.73 | 34.24 |
| | | Mean | | | 2497.5 | | | | | Mean | | | 2826.9 | | | | | Mean | | | 2988.7 | | |
| | 90 | I | 15.30 | 5.88 | 2836.4 | 31.52 | 31.53 | | 90 | I | 14.90 | 5.89 | 2567.3 | 28.53 | 29.25 | | 90 | I | 14.95 | 6.00 | 2168.6 | 24.10 | 24.18 |
| | | II | 15.56 | 6.01 | 2809.1 | 31.21 | 30.04 | | | II | 14.99 | 6.00 | 3029.3 | 33.66 | 33.68 | | | II | 14.95 | 5.93 | 3390.2 | 37.67 | 38.24 |
| | | III† | 15.46 | 5.95 | 2306.4 | 25.63 | 25.07 | | | III† | 15.01 | 5.96 | 2683.3 | 29.81 | 29.99 | | | III† | 15.07 | 5.97 | 3317.2 | 36.86 | 36.87 |
| | | IV | 15.58 | 6.04 | 3025.5 | 33.62 | 32.15 | | | IV | 15.12 | 5.93 | 2842.5 | 31.58 | 31.70 | | | IV | 14.09 | 6.01 | 3443.3 | 38.26 | 40.66 |
| | | V | 15.34 | 5.93 | 2518.8 | 27.99 | 27.69 | | | V | 15.05 | 5.97 | 3301.6 | 36.68 | 36.75 | | | V | 14.97 | 5.99 | 2617.7 | 29.09 | 29.19 |
| | | Mean | | | 2699.2 | | | | | Mean | | | 2884.8 | | | | | Mean | | | 2987.4 | | |
| | 120 | I | 15.10 | 5.90 | 3065.5 | 34.06 | 34.41 | | 120 | I | 15.10 | 5.95 | 3247.9 | 36.09 | 36.15 | | 120 | I | 14.98 | 5.93 | 3382.2 | 37.58 | 38.07 |
| | | II | 15.30 | 6.00 | 3528.4 | 39.20 | 38.44 | | | II | 15.10 | 6.00 | 2976.9 | 33.08 | 32.86 | | | II | 15.07 | 6.42 | 3004.0 | 33.38 | 31.05 |
| | | III† | 15.37 | 6.02 | 2586.0 | 28.73 | 27.95 | | | III† | 15.13 | 6.07 | 2926.2 | 32.51 | 31.86 | | | III† | 15.05 | 5.96 | 3279.6 | 36.44 | 36.56 |
| | | IV | 15.36 | 6.07 | 3372.6 | 37.47 | 36.17 | | | IV | 14.93 | 5.87 | 2857.9 | 31.75 | 32.61 | | | IV | 15.03 | 5.97 | 2869.5 | 31.88 | 31.98 |
| | | V | 15.46 | 5.99 | 3193.8 | 35.49 | 34.49 | | | V | 15.20 | 5.99 | 3381.6 | 37.57 | 37.14 | | | V | 14.91 | 5.97 | 2389.8 | 26.55 | 26.85 |
| | | Mean | | | 3149.3 | | | | | Mean | | | 3078.1 | | | | | Mean | | | 2985.0 | | |

The symbol † identifies, for each series, the tests in which the DIC method was also used.

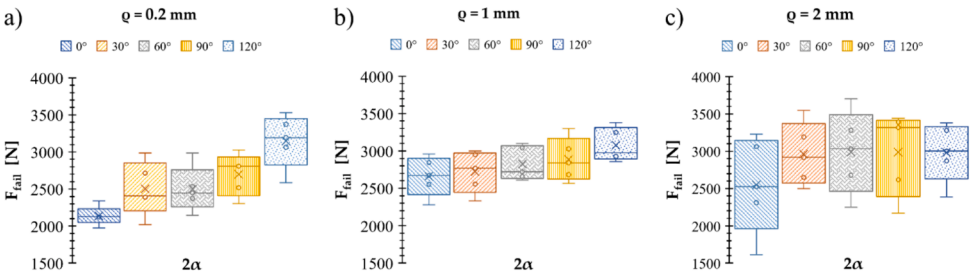


**Fig. 5.** Results of tests on notched specimens as a function of tip radius ρ.

## 4. Discussion

### 4.1. Mechanical properties

The stress versus strain curves in Fig. 2 show the mechanical response of PA12 fabricated via MJF to have a smooth transition from an initial linear elastic behaviour to an irreversible plastic deformation without any highlighted yielding point and a Ramberg-Osgood law can suitably fit this monotonic behaviour. While a phenomenological approach employing the Ramberg-Osgood law is still valuable when aiming to develop analytical models [24], a more accurate constitutive model would require considering both the viscous and the plastic response that thermoplastic polymers, such as PA12, exhibit as well as the mechanical properties' anisotropy that characterize additively manufactured materials [8,30,31].

According to the manufacturer [2], the $\sigma_{UTS}$ should fall within the 45 MPa to 55 MPa range for the 95 % of the cases and the elastic modulus may vary between 1500 and 2100 MPa. Considering $\sigma_{UTS}$, the findings from the experimental campaign lie outside these ranges, as actually also reported in literature [13,23,24,32–34]. Considering the elastic modulus, our findings are inside the range stated by the manufacturer, even though the components printed in the X direction (i.e., flat) showed a stiffer behaviour, while in literature the opposite has also been reported [2,7,35,36]. Regarding the elongation at break, the manufacturer states an $\varepsilon_b$ of 17 % for the X direction and 9 % for the Z one. Considering average values reported in Table 1, our findings where somewhat lower, especially by the horizontally printed samples. However, by looking at the literature an even wider range of values is found, from a minimum of 2.3 % [35] up to 30.0 % [14]. The Poisson's ratio is a far less analysed property in the literature. The manufacturer does not state any range within $\nu$ should fall and our findings indicate average values of 0.4 and 0.36 for X and Z direction respectively. Chen et al. findings indicate that $\nu = 0.4$ for the parts printed in the XY plane [8], Cader et al. stated a 0.372 to 0.409 range without any indication regarding the printing direction [34] and Zolfagharian et al. seem to confirm those results [23]. Looking at other PBF technologies, such as SLS, more studies have been conducted. In [32], SLS PA12 Poisson's ratio turned out to be 0.4068 for the X printing direction and 0.3675 for the Z printing direction; Cano et al. found slightly higher values of 0.43 and 0.407, respectively [37]. These results suggest that Poisson's ratio is less influenced by the PBF technology employed in contrast with the other properties. Such deviation from the ideal values should be expected due to the influence of the testing condition on the results. Moreover, since MJF is still a relatively recent technology, it has not reached the level of standardization of the printing parameters of other PBF technologies such as SLS yet, leading to a higher scatter in the mechanical properties. Considering the deformation and failure process during tensile loading, DIC analyses (see Fig. 10) showed that the specimens, regardless of the building direction, exhibited a uniform strain field up to the 5 % level. Around 7 % strain level, the strain increased locally, at the location where failure finally occurred.

Broken samples featured little to no residual plastic deformation and non-complementarity of the two surfaces. The fracture surfaces looked different for the two building orientations, as shown in Fig. 11 where fracture surfaces refer to specimen broken at lower or higher failure loads.

A more homogeneous look of the X-built samples could be noticed, and, in both printing orientations, the fracture surface associated with lower failure load case appeared to have more significant defects and porosity, with even an evident void in the X-built one. A certain amount of stress whitening is visible on all surfaces, even though it is less evident in the Z-built specimens, which agrees with the stress vs strain charts where they show a less ductile behaviour. It should be remarked that the formation of defects, such as voids and imperfections, is nearly inevitable during the 3D-printing process. For MJF, typical defects include intralayer porosity, voids, and non-processed powders. Intralayer porosity may be created in powder bed fusion processing, mainly during the sintering stage of the powder particles, as a result of poor fusing of powder particles, which produces later empty spaces in the print structure. Single, non-processed, PA12 powder particles may include completely nonmelted and almost melted powder. This may be related to a lack of or nonhomogeneous injection of detailing agent, which could, in turn, locally affect the melting and fusing process in MJF [38].

### 4.2. Mechanical behaviour of the notched samples

Looking at the results of tests carried on the notched samples presented in Fig. 5 and Table 2, some considerations about the mechanical behaviour of MJF PA12 in the presence of notches may be derived. Looking at $\rho = 0.2$ mm specimens, higher sensitivity to the variation on notch opening angle is displayed with less scattered values and a constant increase of failure load when going from 0° to 120°. Larger notch radius configurations seem to generate a more constant $F_{fail}$ values at the increase of 2α, with higher scatter.

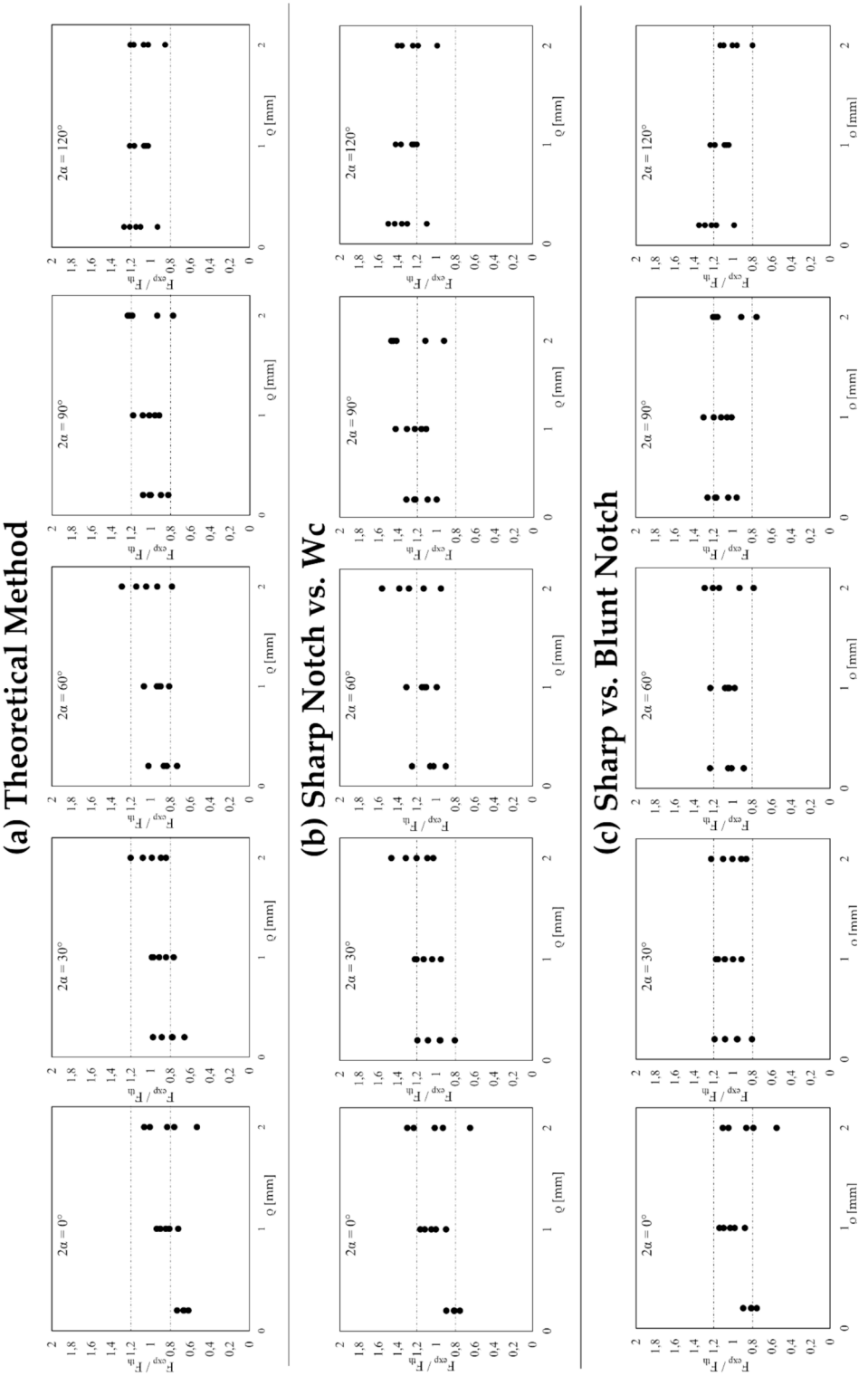


**Fig. 6.** Comparison of experimental and theoretical results for the notched samples as a function of ASED calculation method.

The $\rho = 2$ mm displayed a nearly constant trend of the failure load among the various geometrical group. A possible explanation for this behaviour is related to defects and porosity; as expected from any AM technology, a certain degree of such imperfections at micro-structural level, as mentioned above, is visible on the fracture surfaces; their distribution looks unrelated to the notch geometry. As a

**Table 3**
Prediction of failure load with ASED criterion (ELSE = Total elastic strain energy in the elements of the control volume in FE model, EVOL = Current elements volume).

| (a) Theoretical Method | | | | | | | |
|---|---|---|---|---|---|---|---|
| ρ mm | 2α deg | q | $r_0$ mm | ELSE N mm | EVOL $mm^3$ | $W_{fea}$ N mm/$mm^3$ | $F_{theoretical}$ N |
| 0.2 | 0 | 2.00 | 0.1 | 8.16E-07 | 17.49 | 4.66E-08 | 3193.99 |
| | 30 | 1.83 | 0.091 | 8.08E-07 | 15.94 | 5.07E-08 | 3063.61 |
| | 60 | 1.67 | 0.08 | 8.02E-07 | 14.41 | 5.56E-08 | 2924.16 |
| | 90 | 1.50 | 0.067 | 7.83E-07 | 12.90 | 6.07E-08 | 2798.77 |
| | 120 | 1.33 | 0.05 | 7.01E-07 | 11.38 | 6.16E-08 | 2778.40 |
| 1 | 0 | 2.00 | 0.5 | 9.29E-07 | 19.44 | 4.78E-08 | 3154.69 |
| | 30 | 1.83 | 0.455 | 9.14E-07 | 17.70 | 5.16E-08 | 3034.75 |
| | 60 | 1.67 | 0.4 | 8.97E-07 | 15.95 | 5.62E-08 | 2908.61 |
| | 90 | 1.50 | 0.333 | 8.61E-07 | 14.18 | 6.08E-08 | 2797.80 |
| | 120 | 1.33 | 0.25 | 7.56E-07 | 12.34 | 6.13E-08 | 2786.23 |
| 2 | 0 | 2.00 | 1 | 1.05E-06 | 20.34 | 5.16E-08 | 3035.14 |
| | 30 | 1.83 | 0.909 | 1.03E-06 | 18.81 | 5.45E-08 | 2953.19 |
| | 60 | 1.67 | 0.8 | 9.94E-07 | 17.16 | 5.79E-08 | 2866.31 |
| | 90 | 1.50 | 0.667 | 9.37E-07 | 15.36 | 6.10E-08 | 2791.32 |
| | 120 | 1.33 | 0.5 | 8.09E-07 | 13.33 | 6.07E-08 | 2799.73 |
| (b) Sharp notch vs $W_c$ | | | | | | | |
| ρ mm | 2α deg | q | $r_0$ mm | ELSE N mm | EVOL $mm^3$ | $W_{fea}$ N mm/$mm^3$ | $F_{theoretical}$ N |
| 0.2 | 0 | 2.00 | 0.1 | 5.22E-07 | 7.47 | 6.98E-08 | 2609.98 |
| | 30 | 1.83 | 0.091 | 5.16E-07 | 6.80 | 7.59E-08 | 2502.98 |
| | 60 | 1.67 | 0.08 | 5.11E-07 | 6.13 | 8.33E-08 | 2389.98 |
| | 90 | 1.50 | 0.067 | 4.89E-07 | 5.48 | 8.92E-08 | 2308.73 |
| | 120 | 1.33 | 0.05 | 4.12E-07 | 4.82 | 8.55E-08 | 2358.53 |
| 1 | 0 | 2.00 | 0.5 | 6.19E-07 | 8.37 | 7.39E-08 | 2536.27 |
| | 30 | 1.83 | 0.455 | 6.06E-07 | 7.69 | 7.89E-08 | 2455.14 |
| | 60 | 1.67 | 0.4 | 5.88E-07 | 6.97 | 8.44E-08 | 2373.93 |
| | 90 | 1.50 | 0.333 | 5.49E-07 | 6.21 | 8.83E-08 | 2320.69 |
| | 120 | 1.33 | 0.25 | 4.52E-07 | 5.40 | 8.39E-08 | 2381.42 |
| 2 | 0 | 2.00 | 1 | 6.98E-07 | 9.02 | 7.74E-08 | 2478.65 |
| | 30 | 1.83 | 0.909 | 6.75E-07 | 8.35 | 8.08E-08 | 2425.51 |
| | 60 | 1.67 | 0.8 | 6.44E-07 | 7.63 | 8.44E-08 | 2374.41 |
| | 90 | 1.50 | 0.667 | 5.92E-07 | 6.86 | 8.63E-08 | 2347.29 |
| | 120 | 1.33 | 0.5 | 4.85E-07 | 5.96 | 8.13E-08 | 2418.34 |
| (c) Sharp notch vs blunt notch | | | | | | | |
| ρ mm | 2α deg | q | $r_0$ mm | ELSE N mm | EVOL $mm^3$ | $W_{fea}$ N mm/$mm^3$ | $F_{theoretical}$ N |
| 0.2 | 0 | 2.00 | 0.1 | 2.13E-07 | 1.23 | 1.73E-07 | 2610.18 |
| | 30 | 1.83 | 0.091 | 2.10E-07 | 1.12 | 1.88E-07 | 2503.70 |
| | 60 | 1.67 | 0.08 | 2.04E-07 | 1.01 | 2.03E-07 | 2411.38 |
| | 90 | 1.50 | 0.067 | 1.83E-07 | 0.89 | 2.05E-07 | 2398.17 |
| | 120 | 1.33 | 0.05 | 1.34E-07 | 0.78 | 1.72E-07 | 2613.54 |
| 1 | 0 | 2.00 | 0.5 | 2.57E-07 | 1.47 | 1.75E-07 | 2591.79 |
| | 30 | 1.83 | 0.455 | 2.46E-07 | 1.36 | 1.81E-07 | 2550.31 |
| | 60 | 1.67 | 0.4 | 2.30E-07 | 1.24 | 1.86E-07 | 2516.72 |
| | 90 | 1.50 | 0.333 | 2.03E-07 | 1.11 | 1.84E-07 | 2532.12 |
| | 120 | 1.33 | 0.25 | 1.51E-07 | 0.96 | 1.57E-07 | 2736.97 |
| 2 | 0 | 2.00 | 1 | 2.51E-07 | 1.82 | 1.38E-07 | 2921.01 |
| | 30 | 1.83 | 0.909 | 2.36E-07 | 1.67 | 1.41E-07 | 2892.34 |
| | 60 | 1.67 | 0.8 | 2.17E-07 | 1.52 | 1.43E-07 | 2866.05 |
| | 90 | 1.50 | 0.667 | 1.93E-07 | 1.34 | 1.44E-07 | 2861.70 |
| | 120 | 1.33 | 0.5 | 1.51E-07 | 1.14 | 1.32E-07 | 2984.47 |

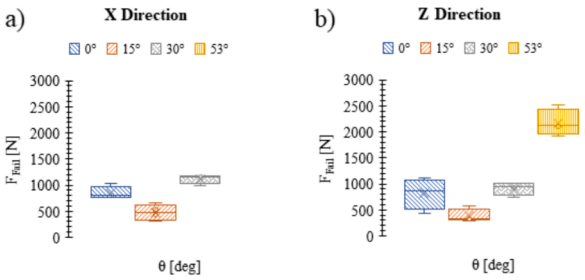


**Fig. 7.** (a), (b) Failure loads for SCB samples for printing direction X and Z.

**Table 4**
Experimental result of semi-circular bend specimens.

| Orientation | θ deg | Nr. | $F_{fail}$ N | Orientation | θ deg | Nr. | $F_{fail}$ N |
|---|---|---|---|---|---|---|---|
| XY | 0 | I | 753.83 | Z | 0 | I | 735.38 |
| | | II | 844.05 | | | II | 430.72 |
| | | III[a] | 777.79 | | | III[a] | 1108.41 |
| | | IV[a] | 1024.53 | | | IV[a] | 992.64 |
| | | Mean | 850.05 | | | Mean | 816.79 |
| | | St.D. | 122.41 | | | St.D. | 300.91 |
| | 15 | I | 651.25 | | 15 | I | 340.57 |
| | | II | 428.28 | | | II | 337.72 |
| | | III[a] | 305.19 | | | III[a] | 293.95 |
| | | IV[a] | 527.10 | | | IV[a] | 572.45 |
| | | Mean | 477.96 | | | Mean | 386.17 |
| | | St.D. | 146.93 | | | St.D. | 126.00 |
| | 30 | I | 1174.16 | | 30 | I | 952.78 |
| | | II | 1165.87 | | | II | 934.60 |
| | | III[a] | 1152.98 | | | III[a] | 739.40 |
| | | IV[a] | 987.97 | | | IV[a] | 1018.58 |
| | | Mean | 1120.24 | | | Mean | 911.34 |
| | | St.D. | 88.61 | | | St.D. | 120.17 |
| | 53 | I | | | 53 | I | 1908.51 |
| | | II | | | | II | 2096.42 |
| | | III | | | | III[a] | 2162.07 |
| | | IV | | | | IV[a] | 2512.36 |
| | | Mean | | | | Mean | 2169.84 |
| | | St.D. | | | | St.D. | 252.36 |

[a] Tested with DIC. Ductile failure.

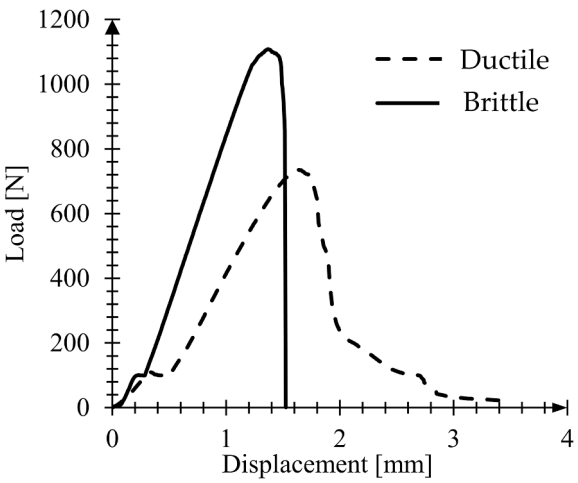


**Fig. 8.** Example of ductile or brittle failure behaviour.

**Table 5**
Theoretical results for semi-circular bend sample (ELSE = Total elastic strain energy in the elements of the control volume in FE model EVOL = Current elements volume).

| Orientation | θ deg | ELSE N mm | EVOL $mm^3$ | $W_{fea}$ N mm/$mm^3$ | $F_{theoretical}$ N |
|---|---|---|---|---|---|
| XY | 0 | 1.49E-05 | 21.32 | 6.98E-07 | 825.35 |
| | 15 | 1.26E-05 | 21.32 | 5.93E-07 | 895.89 |
| | 30 | 8.01E-06 | 21.32 | 3.76E-07 | 1125.17 |
| | 53 | 2.52E-06 | 21.32 | 1.18E-07 | 2004.65 |
| Z | 0 | 2.14E-05 | 33.34 | 6.41E-07 | 861.58 |
| | 15 | 1.81E-05 | 33.34 | 5.42E-07 | 936.92 |
| | 30 | 1.14E-05 | 33.34 | 3.41E-07 | 1180.64 |
| | 53 | 3.60E-06 | 33.34 | 1.08E-07 | 2098.56 |

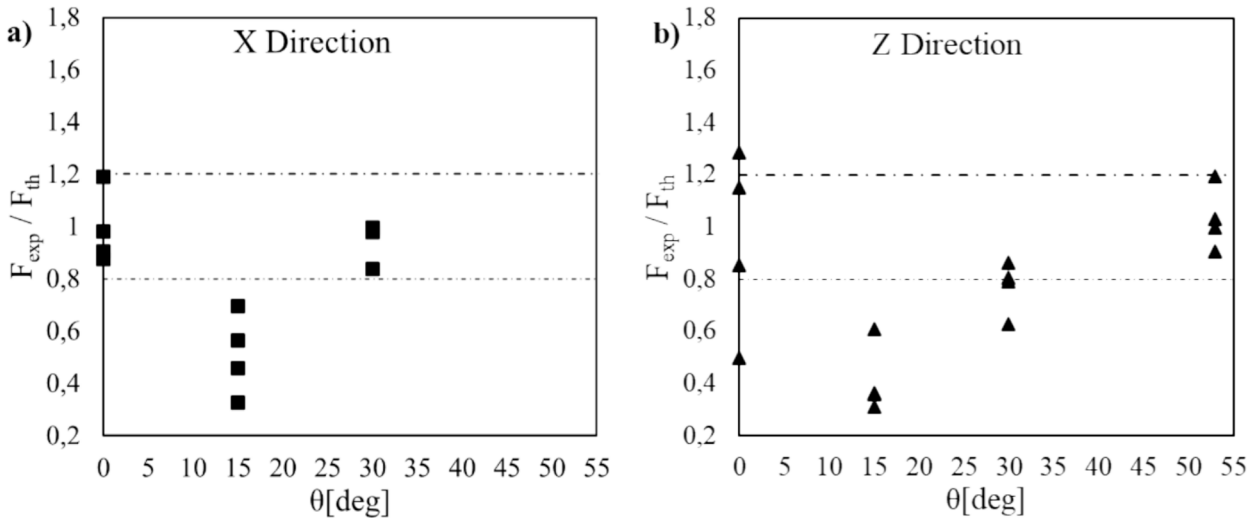


**Fig. 9.** Comparison between experimental and theoretical failure loads for semi-circular bend samples (a) X direction (b) Z direction.

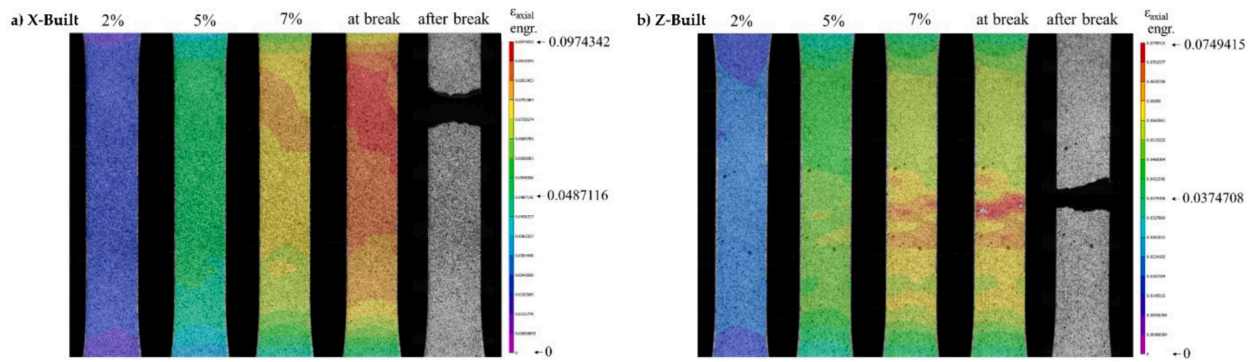


**Fig. 10.** Representative strain fields during tensile tests from DIC analysis a) X-Built, b) Z-Built specimens.

result, while in the smallest notch radius the effect of defects may be covered by the severity of the geometrical discontinuity, at the increase of ρ, their influence over the $F_{fail}$ may increase to the point where the sensitivity of the results on the geometrical features is almost nullified. Inside the same ρ-2α configuration, the degree of defects and porosity is also related to the various failure load registered and, consequently, to the scatter of the results. For example, considering the ρ = 1 mm-2α = 60° configuration, the lowest failure load occurred in a specimen having larger defects, which causes a more pronounced reduction of net resistance section.

Overall, the fracture surfaces presented similar features and the classical ductile failure appearance with low plastic deformation and stress whitening, particularly around the notch tip where higher local stresses are located. Considering crack propagation various

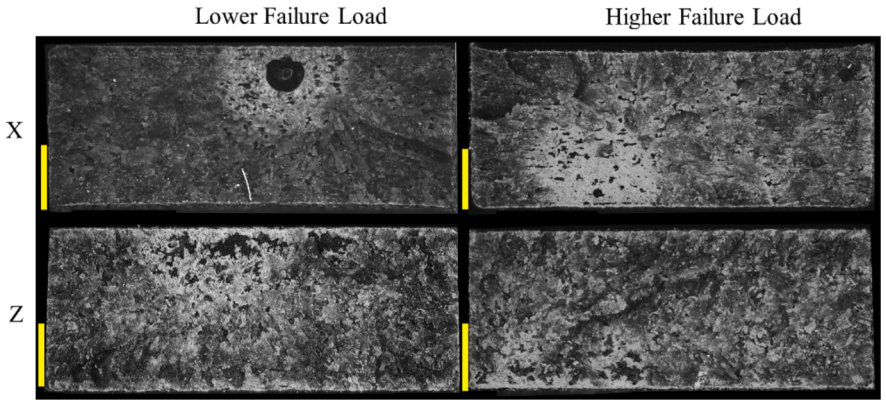


**Fig. 11.** Fracture surfaces of dogbone specimens for lower and higher failure loads, as a function on printing orientation (yellow line marker 2.5 mm). (For interpretation of the references to colour in this figure legend, the reader is referred to the web version of this article.)

behaviours were displayed, as shown in Fig. 12, which do not seem to be related to any particular notch geometry.

In some cases, the crack propagated along the notch bisector, but failure with crack deviation from notch bisector line also occurred, as well as crack path splitting into two branches, with a piece of material remaining inside.

Considering the DIC results a similar pattern is shown by each configuration (see Fig. 13) for a representative example), with an as-expected concentration of the strain around the notch tip, quite symmetrical in respect of both the notch bisector line and the left and the right side of the specimens. The shape of the higher strain area typically assumes a "C" shape, leaving a lower strain region in the middle part of the notch bisector line. A partial exception to this response could be noticed for some of the $\rho = 2$ mm samples, with a slight deviation from the typical pattern and the highest strain zone positioned asymmetrically, probably due to the higher weight of the defects over the mechanical response already highlighted before.

### *4.3. Mixed mode fracture behaviour obtained from semi-circular bend samples*

A representative example of DIC strain patterns is available in Fig. 14. In general, a peak of the maximal principal strain near the crack tip could be noticed, as well as a minimum in the area directed toward the upper roller, where also the peak of the minimum principal strain is located; the minimum of this latter quantity is directly underneath the upper roller.

An exception to this pattern was found for the $\theta = 53^{\circ}$, where no particular strain distribution was visible towards the force application point.

Looking at the results of SCB tests, the samples showed two distinct behaviours at the fracture: brittle and ductile. There is no evidence of a correlation between the printing direction and the type of failure displayed, 33 % of the X-built samples failed in a ductile fashion while, for Z-built ones, the percentage is 37.5 %. The same thing cannot be said about the correlation between crack angle and ductile behaviour at failure; in fact, 70 % of the ductily failed samples belong to the 15° crack angle configurations. This value of crack angle also displays another unexpected behaviour. Increasing the crack angle, it is common sense that the failure load should also increase, as already stated by [39–42]. While most of examined configurations followed the expected trend, with the failure load increasing at the higher crack angles, our findings disagree with this behavior, being the 15° the weakest angle. The reason behind such a trend of $F_{fail}$ are not entirely clear, as no evidence of different defect size or type was noticed for this particular set of specimens. Various hypotheses have been made. A first possible cause could be that during the preparation of the specimens, the blade may have cracked them more than required, creating a longer crack. Such a hypothesis is likely refuted by the dimensional checks. Actually, even though in the X case the crack angle of interest displayed averagely longer cracks, the same thing did not happen in the Z one, where the 15° has even the smaller error of all the four configurations. A second aspect to be considered, which is closely related to the previous one, is that the measurement of each crack was executed after the breakage of the sample. In fact, the cut-through surface appearance is uniform and glossy, compared to the fracture surface, which is rough and uneven, making the measurement easier. It might have happened that during the cracking procedure, the blade reached the desired depth inside the material, but a partial fracture was also created at the crack tip, elongating the crack itself without being detectable retrospectively during the dimensional check. To further investigate possible pre-cracking damage SCB fracture surfaces were observed with optical microscopy (LEICA DMS 300). Some representative examples of the different types of fracture surface aspect in the pre-cracked region are shown in the Fig. 15.

In general no whitening zones ahead of the pre-cracks could be found on the pre-cracked specimens, but in some cases some damage could be detected. While most of the specimens that exhibited brittle failure were characterized by a clear cut at the tip of the crack (as in Fig. 15(a)), for the 15° angle configuration the specimens actually featured more irregular end (Fig. 15(b)), which could be related to the ductile behaviour observed at macroscopical level. However, also some of the specimens that were qualified as brittle exhibited a similar aspect (see Fig. 15(c), so ex-post it is difficult to understand whether ductile response, mostly observed for 15° configuration, is exclusively related to a pre-crack damage or to some specific failure mechanism of MJF PA12 elicited with this angle. Overall, the X building orientation performed better, confirming the results from the plain dogbone tensile tests. In all the cases, the crack propagated

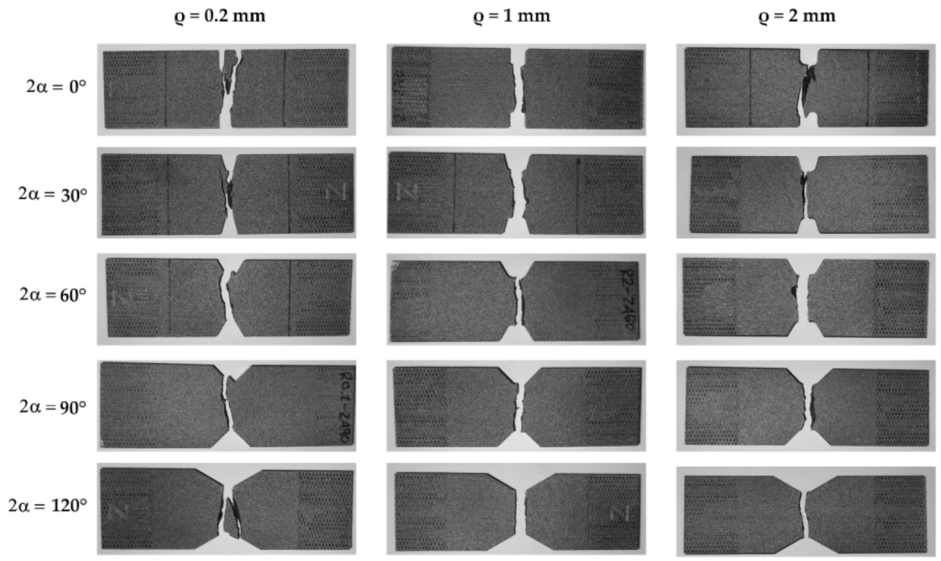


**Fig. 12.** Crack propagation, side view of broken notched samples for tested combinations of opening angles and tip radius.

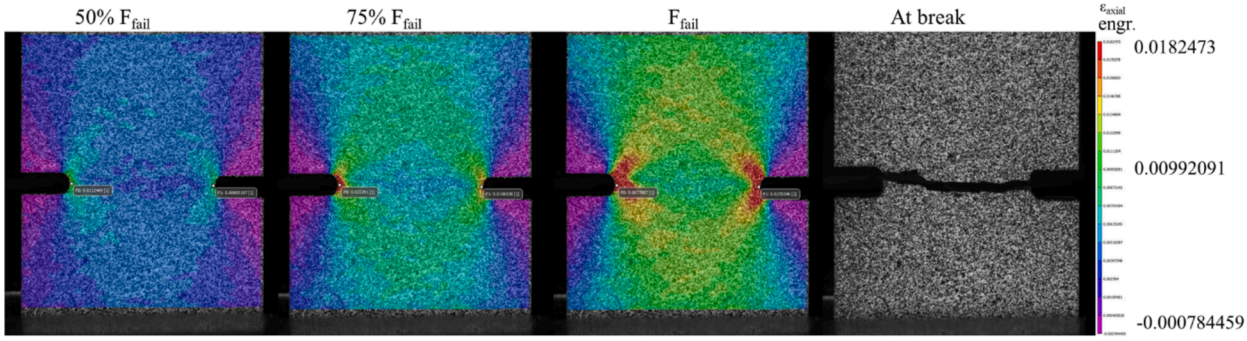


**Fig. 13.** Example of representative strain fields during tensile tests from DIC analysis ($\rho = 1$ mm,$2\alpha = 0°$ specimen).

toward the upper roller, while in few cases a small propagation along the pre-crack was observed followed by the propagation towards the top roller. The DIC acquisitions showed that quite independently from the building direction and the crack angle, all the specimens' strain fields were similar.

### *4.4. Average strain energy criterion applicability to MJF PA12*

The theoretical results from the ASED criterion look overall accurate. Three different calibration methods were used in different cases based on the available data from the mechanical tests, as shown in Fig. 4 for notched configuration and in Fig. 5 for SCB. Taking a closer look at results from the standard approach employing the theoretical formulation, the worst prediction concerns the $\rho = 0.2$ mm $- 2\alpha = 0°$ configuration, in which all the samples exhibited lower $F_{fail}$ that the predicted value. This can be critical due to the overestimation of the performance, leading to unpredicted breakdowns. The agreement between the theoretical and experimental results improves at more prominent notch opening angles. On average, the criterion provides results on the safety side, underestimating the actual failure load of most of the samples while still being inside the $\pm$ 20 %. Regarding the two alternative methods presented, the "sharp notch vs. $W_c$" approach provided mostly underestimated failure load values, especially at a larger notch tip radius and opening angle. If, from one point of view, this can be detrimental to the optimization of the resistance/weight ratio of the final component, it has to be considered that for MJF, especially for newer printer models, the optimization of printing parameters is still a research topic. An underestimation of fracture strength may thus provide an extra safety condition to account for the relatively high scatter of the obtained mechanical performance which is still observed. The "sharp vs. blunt notch" approach has the main advantage of requiring testing only two different notched sample geometries resulting in a faster and less expensive way to apply the criterion. The prediction is reliable, with just a few cases of overestimated outliers. As regards the SCB specimens, in both building directions, the failure load prediction is reliable besides the $\theta = 15°$ samples, where the criterion does not predict the decreased performance compared to the pure mode I case. Overall, we can conclude that the ASED criterion provides a practical and simple tool

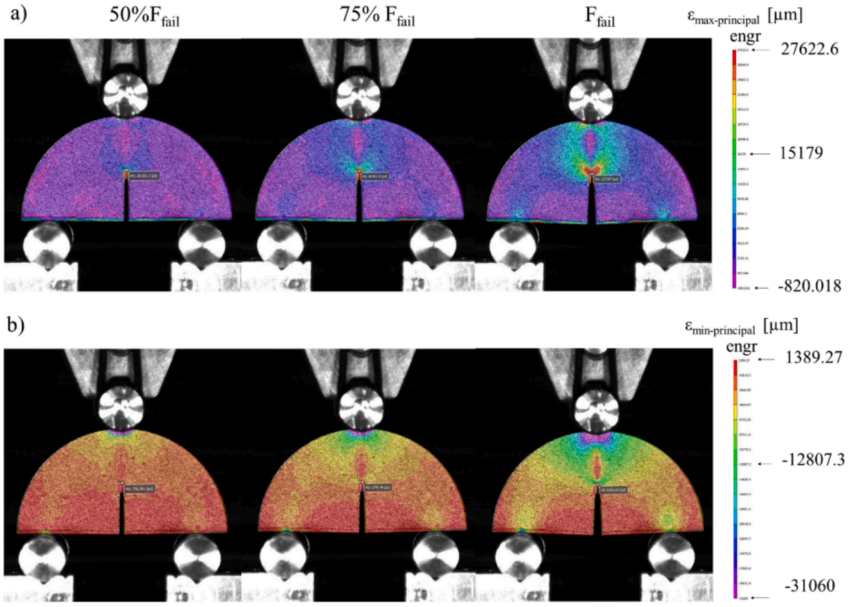


**Fig. 14.** Example of representative strain fields during tensile tests from DIC analysis (X-built, $\theta = 0°$ SCB specimen).

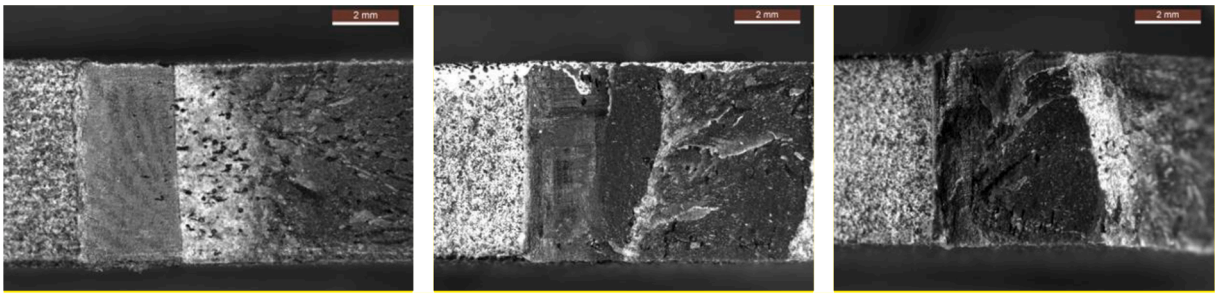


**Fig. 15.** Optical Microscopy on fracture surfaces (a) X-0°, Brittle failure, (b) Z-25°, Ductile failure, (a) Z-30°, Brittle failure.

to predict the performance of notched and cracked components in MJF − PA12. However, caution is required during the design phase, where significant safety factors may be employed to compensate for the mechanical performance's inherent variability.

## 5. Conclusions

In this paper, a fracture assessment of PA12 fabricated via MJF in the presence of geometrical discontinuities has been executed considering various geometrical combinations of notched specimens as well as different combinations of mode mixity and building orientation of SCB ones. This has been accomplished by integrating results from mechanical tests, eventually employing DIC, and theoretical ones from ASED criterion and FEA. Tests conducted on the plain dogbone specimens have shown the mechanical behaviour of MJF fabricated PA12 to have: i) an initial elastic behaviour followed by a smooth transition −without an obvious yielding point − into a plastic one with irreversible deformations; ii) a slightly anisotropic behaviour. Overall, the mechanical properties were comparable to those of PA12 manufactured with conventional methods in terms of Young's modulus and strength. However, the scatter observed in experimental tests also supports the conclusion that for full exploitation of the potential of this versatile and promising technology more studies are needed to reach a higher level of replicability.

When it comes to notched components, the sensitivity to the notch opening angle diminishes at the increase of the notch tip radius, namely, the blunter the notch, the lesser the failure load is influenced by it. The weight of the defects increases to the point where the $\rho = 2$ mm configuration displayed a nearly constant average failure load, and the highest one has been registered at $2\alpha = 60°$. Coming to the SCB specimens, two distinct behaviours at fracture, brittle and ductile, were displayed. These different failure conducts appeared to be related to the crack angle independently from the building direction considered. Regarding the crack angle, the $\theta = 15°$ configuration showed the worst performances in both printing orientations, contrary to what was expected. Lastly, applying the ASED

criterion has demonstrated this theory as a simple and practical approach to assessing the load capacity of notched and cracked components.

## CRediT authorship contribution statement

**Andrea Avanzini:** Conceptualization, Methodology, Project administration, Resources, Supervision, Validation, Writing – original draft. **Matteo Tomasoni:** Data curation, Formal analysis, Investigation, Validation, Visualization, Writing – original draft. **Zhuo Xu:** Formal analysis, Methodology. **Filippo Berto:** Supervision, Validation, Writing – review & editing. **Nima Razavi:** Conceptualization, Methodology, Project administration, Resources, Supervision, Validation. Writing – review & editing.

## Declaration of competing interest

The authors declare that they have no known competing financial interests or personal relationships that could have appeared to influence the work reported in this paper.

## Data availability

Data will be made available on request.

## Acknowledgements

The authors would like to thank Antonio Vulcano and ELMEC 3D S.p.A for their support to the research by providing samples and information on the process.

## References

[1] Iso, astm52900-21,. Standard Terminology for Additive Manufacturing – General Principles – Terminology (ASTM52900). Int Organ Stand Geneva Switz 2021:1–28.
[2] Hewlett-Packard©, HP 3D Printing materials for the HP Jet Fusion 4200 3D Printing Solution; 2020, https://h20195.www2.hp.com/v2/GetDocument.aspx?docname=4AA7-7085ENW (accessed 03/03/2023).
[3] Vasquez GM, Majewski CE, Haworth B, Hopkinson N. A targeted material selection process for polymers in laser sintering. Additive Manufacturing 2014;1:127–38. https://doi.org/10.1016/j.addma.2014.09.003.
[4] Yuan S, Shen F, Chua CK, Zhou K. Polymeric composites for powder-based additive manufacturing: materials and applications. Prog Polym Sci 2019;91:141–68. https://doi.org/10.1016/j.progpolymsci.2018.11.001.
[5] Tan LJ, Zhu W, Zhou K. Recent progress on polymer materials for additive manufacturing. Adv Funct Mater 2020;30:2003062. https://doi.org/10.1002/adfm.202003062.
[6] Ali M, Sari RK, Sajjad U, Sultan M, Ali HM. Effect of annealing on microstructures and mechanical properties of PA-12 lattice structures proceeded by multi jet fusion technology. Addit Manuf 2021;47:102285. https://doi.org/10.1016/j.addma.2021.102285.
[7] O'Connor HJ, Dickson AN, Dowling DP. Evaluation of the mechanical performance of polymer parts fabricated using a production scale multi jet fusion printing process. Addit Manuf 2018;22:381–7. https://doi.org/10.1016/j.addma.2018.05.035.
[8] Chen K, et al. Experimental and modeling investigation on the viscoelastic-viscoplastic deformation of polyamide 12 printed by Multi Jet Fusion. Int J Plast 2021;143:103029. https://doi.org/10.1016/j.ijplas.2021.103029.
[9] Srinivas RP, et al. Mechanical response of a compressed novel 3D tetrachiral structure processed by MJF 3D printing process. Mater Today: Proc 2021;46:4776–81. https://doi.org/10.1016/j.matpr.2020.10.312.
[10] O'Connor HJ, Dowling DP. Comparison between the properties of polyamide 12 and glass bead filled polyamide 12 using the multi jet fusion printing process. Addit Manuf 2020;31:100961. https://doi.org/10.1016/j.addma.2019.100961.
[11] Riedelbauch J, Rietzel D, Witt G. Analysis of material aging and the influence on the mechanical properties of polyamide 12 in the Multi Jet Fusion process. Addit Manuf 2019;27:259–66. https://doi.org/10.1016/j.addma.2019.03.002.
[12] Osswald PV, Osswald TA. A strength tensor based failure criterion with stress interactions. Polym Compos 2018;39:2826–34. https://doi.org/10.1002/pc.24275.
[13] Osswald PV, et al. Failure criterion for PA 12 multi-jet fusion additive manufactured parts. Addit Manuf 2021;37:101668. https://doi.org/10.1016/j.addma.2020.101668.
[14] Rosso S, et al. In-depth comparison of polyamide 12 parts manufactured by multi jet fusion and selective laser sintering. Addit Manuf 2020;36:101713. https://doi.org/10.1016/j.addma.2020.101713.
[15] Palma T, et al. Multiscale mechanical and tribological characterizations of additively manufactured polyamide 12 parts with different print orientations. J Manuf Process 2019;40:76–83. https://doi.org/10.1016/j.jmapro.2019.03.004.
[16] Ameri, B., Taheri-behrooz, F., Majidi, H. R., Mixed-mode load bearing estimation of the cracked additively manufactured materials using stress / strain-based models, **2**, 218–231 (2023). doi: 10.1108/RPJ-11-2021-0316.
[17] Shahbaz S, Ayatollahi MR, Petru M, Torabi AR. U-notch fracture in additively manufactured ABS specimens under symmetric three-point bending. Theor Appl Fract Mech 2022;119(March):103318. https://doi.org/10.1016/j.tafmec.2022.103318.
[18] Torabi AR, Shahbaz S, Ayatollahi MR. Fracture assessment of U-notched diagonally loaded square plates additively manufactured from ABS with different raster orientations. Engng Struct 2023;292(June):116537. https://doi.org/10.1016/j.engstruct.2023.116537.
[19] Ameri B, Taheri-Behrooz F, Aliha MRM. Evaluation of the geometrical discontinuity effect on mixed-mode I/II fracture load of FDM 3D-printed parts. Theor Appl Fract Mech 2021;113(March):102953. https://doi.org/10.1016/j.tafmec.2021.102953.
[20] Crespo M, Río MTG, Rodríguez J. Failure of SLS polyamide 12 notched samples at high loading rates. Theor Appl Fract Mech 2017;92(July):233–9. https://doi.org/10.1016/j.tafmec.2017.08.008.
[21] Cano AJ, Salazar A, Rodríguez J. Effect of temperature on the fracture behavior of polyamide 12 and glass-filled polyamide 12 processed by selective laser sintering. Engng Fract Mech 2018;203:66–80. https://doi.org/10.1016/j.engfracmech.2018.07.035.
[22] Zehir B, Seyedzavvar M, Boga C. Exploring mixed-mode fracture behavior and mechanical properties of selective laser sintered polyamide 12 components'. Rapid Prototyp J 2024;30(3):529–46. https://doi.org/10.1108/RPJ-08-2023-0270.

[23] Zolfagharian A, Khosravani MR, Kaynak A. Fracture resistance analysis of 3D-printed polymers. Polymers 2020;12:1–18. https://doi.org/10.3390/polym12020302.
[24] Avanzini A, Battini D, Pandini S. Static and fatigue behavior in presence of notches for polyamide 12 (PA12) additively manufactured via Multi Jet Fusion™ process. Int J Fatigue 2022;161:106912. https://doi.org/10.1016/j.ijfatigue.2022.106912.
[25] Abbott CS, Sperry M, Crane NB. Relationships between porosity and mechanical properties of polyamide 12 parts produced using the laser sintering and multi-jet fusion powder bed fusion processes. J Manuf Process 2021;70:55–66. https://doi.org/10.1016/j.jmapro.2021.08.012.
[26] Berto F, Lazzarin P. A review of the volume-based strain energy density approach applied to V-notches and welded structures. Theor Appl Fract Mech 2009;52:183–94. https://doi.org/10.1016/j.tafmec.2009.10.001.
[27] Berto F, Lazzarin P. Recent developments in brittle and quasi-brittle failure assessment of engineering materials by means of local approaches. Mater Sci Engng R Rep 2014;75:1–48. https://doi.org/10.1016/j.mser.2013.11.001.
[28] Razavi SMJ, Aliha MRA, Berto F. Application of an average strain energy density criterion to obtain the mixed mode fracture load of granite rock tested with the cracked asymmetric four-point bend specimens. Theor Appl Fract Mech 2018;97:419–25. https://doi.org/10.1016/j.tafmec.2017.07.004.
[29] Dowling, N.E., Mechanical behavior of materials: Engineering methods for deformation, fracture and fatigue (4th Ed.) 644-645 (Pearson, 2013).
[30] Sagradov I, et al. Experimental investigation and numerical modelling of 3D printed polyamide 12 with viscoplasticity and a crack model at different strain rates. Mater Today Commun 2020;25:101542. https://doi.org/10.1016/j.mtcomm.2020.101542.
[31] Lammens N, Kersemans M, De Baere I, Van Paepegem W. On the visco-elasto-plastic response of additively manufactured polyamide-12 (PA-12) through selective laser sintering. Polym Test 2017;57:149–55. https://doi.org/10.1016/j.polymertesting.2016.11.032.
[32] Galati M, Calignano F, Defanti S, Denti L. Disclosing the build-up mechanisms of multi jet fusion: Experimental insight into the characteristics of starting materials and finished parts. J Manuf Process 2020;57:244–53. https://doi.org/10.1016/j.jmapro.2020.06.029.
[33] Xu Z, Wang Y, Wu D, Prem Ananth K, Bai J. The process and performance comparison of polyamide 12 manufactured by multi jet fusion and selective laser sintering. J Manuf Process 2019;47:419–26. https://doi.org/10.1016/j.jmapro.2019.07.014.
[34] Cader M, Kiński W. Effect of Changing the Parameters of the Multi Jet Fusion (MJF) Process on the Spatial Objects Produced. Problems of Mechatronics Armament Aviation Safety Engineering 2020;11(4):61–72. https://doi.org/10.5604/01.3001.0014.5644.
[35] Morales-Planas S, Minguella-Canela J, Lluma-Fuentes J, Travieso-Rodriguez JA, García-Granada AA. Multi Jet Fusion PA12 manufacturing parameters for watertightness, strength and tolerances. Materials 2018;11(8):1–11. https://doi.org/10.3390/ma11081472.
[36] Cai C, et al. Comparative study on 3D printing of polyamide 12 by selective laser sintering and multi jet fusion. J Mater Process Technol 2021;288:116882. https://doi.org/10.1016/j.jmatprotec.2020.116882.
[37] Cano AJ, Salazar A, Rodríguez J. Effect of the orientation on the fatigue crack growth of polyamide 12 manufactured by selective laser sintering. Rapid Prototyp J 2019;25(5):820–9. https://doi.org/10.1108/RPJ-09-2018-0255.
[38] Adach M, Sokolowski P, Piwowarczyk T, Nowak K. Study on geometry dimensional accuracy and structure of parts produced by multi jet fusion. Materials 2021;14:4510. https://doi.org/10.3390/ma14164510.
[39] Ayatollahi MR, Aliha MRM, Hassani MM. Mixed mode brittle fracture in PMMA—an experimental study using SCB specimens. Mater Sci Engng A 2006;417:348–56. https://doi.org/10.1016/j.msea.2005.11.002.
[40] Ayatollahi MR, Nabavi-Kivi A, Bahrami B, Yahya MY, Khosravani MR. The influence of in-plane raster angle on tensile and fracture strengths of 3D-printed PLA specimens. Engng Fract Mech 2020;237:107225. https://doi.org/10.1016/j.engfracmech.2020.107225.
[41] Nabavi-Kivi A, Ayatollahi MR, Rezaeian P, Razavi SMJ. Investigating the effect of printing speed and mode mixity on the fracture behavior of FDM-ABS specimens. Theor Appl Fract Mech 2022;118:103223. https://doi.org/10.1016/j.tafmec.2021.103223.
[42] Bahrami B, Ayatollahi MR, Sedighi I, Pérez MA, Garcia-Granada AA. The effect of in-plane layer orientation on mixed-mode I-II fracture behavior of 3D-printed poly-carbonate specimens. Engng Fract Mech 2020;231:107018. https://doi.org/10.1016/j.engfracmech.2020.107018.